Source Characterisitics of the Largest Three Aftershocks of the 1983 Japan Sea Earthquake

YASUO IZUTANI

Department of Architecture and Civil Engineering, Faculty
of Engineering, Shinshu University, Nagano 380

TOMOWO HIRASAWA

Faculty of Science, Tohoku University, Sendai 980

Abstract : Intermediate–period P-wave records at far-field stations are analyzed to derive the focal depth and the source characteristics of the largest three aftershocks of the Japan Sea earthquake of May 26, 1983. Event A (June 9, 21 : 49, $M_{JMA}=6.1$) and Event B (June 9, 22 : 04, $M_{JMA}=6.0$) occurred near the south edge of the source region of the main shock. Their focal depths are determined as 13 km and 12 km, respectively. Event C (June 21, 15 : 25, $M_{JMA}=7.1$) took place near the north edge of the source region. Its focal depth is estimated at about 8 km. The essential part of moment rate function for Event A is found to be expressed by a single pulse with a width of about 1 sec, while that for Event B is composed of two pulses separated in time. The moment rate function obtained for Event C consists of two pulses with nearly the same width of about 3.5 sec, and the time lag between them is estimated at 2.5 sec.

1. Introduction

It is well-known that major earthquakes along the Japan trench are caused by the relative movement between the Pacific plate and the Japan arc. On the other hand, the relationship between the tectonics and the earthquake occurrence along the eastern margin of the Japan Sea has not been clarified mainly because of the lack of data.

The Japan Sea earthquake of May 26, 1983, surprised seismologists because of its large magnitude ($M_{JMA}=7.7$) and its location. The epicenter is far from the Japan Sea coast of the northern Honshu in comparison with those of historical large earthquakes along the eastern margin of the Japan Sea. Many studies have been carried out to investigate the source characteristics of the main shock (*e.g.*, Shimazaki and Mori, 1983 ; Ishikawa *et al.*, 1984 ; Kanamori and Astiz, 1985 ; Sato, 1985 ; Fukuyama and Irikura, 1986) and the spatial and temporal distribution of the aftershocks (*e.g.*, Umino *et al.*, 1985 ; Urabe *et al.*, 1985 ; Sato *et al.*, 1986 ; Nosaka *et al.*, 1987). The important results of these studies are that the focal mechanism solution shows reverse faulting, and that the eastward dipping fault-plane is distinguished from two P-nodal planes on the basis of the aftershock distribution. It is possible to consider this as a supporting evidence for the hypothesis that the Eurasian plate is subducting beneath the northern Japan from the eastern margin of the Japan Basin (*e.g.*, Nakamura, 1983). Another important result is

that the main shock was a complex multiple event.

For a better understanding of the source characteristics of the main shock it would be important to examine the source process of large aftershocks. Ishikawa *et al.* (1984) and Masuda and Hamaguchi (1988) analyzed far-field long-period seismograms to derive the source process of the largest two aftershocks. In the present study, intermediate-period records by Global Digital Seismograph Network (GDSN) are analyzed to discuss the detailed source process and the focal depth of the largest three aftershocks. Further, we examine some influence of the source process on the characteristics of strong ground motions observed in the near-field.

2. Data and Method of Analysis

Two of the three aftershocks analyzed in this study ocurred on June 9, 1983, in the southern part of the aftershock area as shown in Fig. 1. They are called Event A and Event B henceforth. Their magnitudes by the Japan Meteorological Agency (JMA) are 6.1 and 6.0, respectively. The other one (Event C) is the largest aftershock with JMA magnitude of 7.1, which occurred on June 21 in the northern part of the aftershock area. The origin times and the hypocenter locations by the Tohoku University are listed in
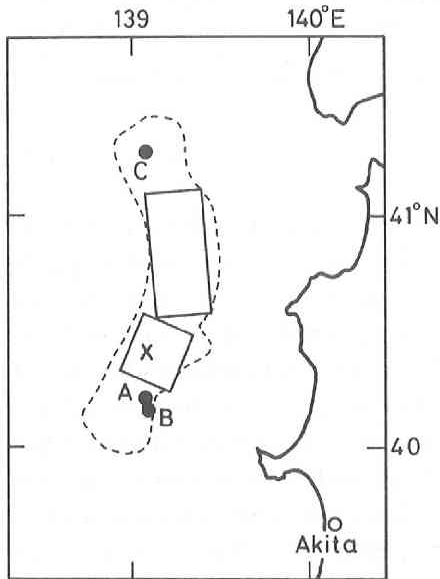

Fig. 1 Epicenters of the three events, A, B and C. The cross and the dashed curve denote the epicenter of the main shock of the 1983 Japan Sea earthquake and the approximate epicentral area of its aftershocks. The rectangles indicate the fault model of the main shock by Shimazaki and Mori (1983).
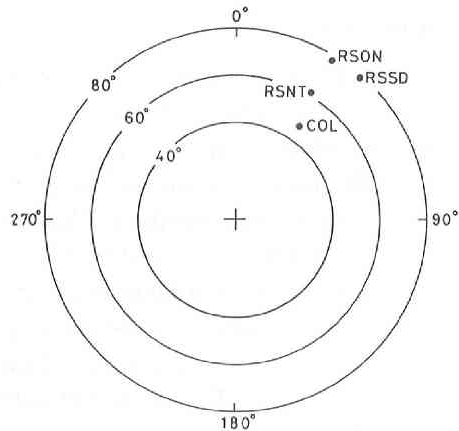
Fig. 2 Station locations relative to the epicentral region of the three events. The cross and the concentric circles denote the epicentral region and the epicentral distance.

Table 1.   Earthquake Data Given by Tohoku University

Event	Date	Origin time (JST)	Latitude (N)	Longitude (E)	Depth (km)	Magnitude (M_{JMA})
A	June 9, 1983	$21^{\mathrm{h}}49^{\mathrm{m}}03.2^{\mathrm{s}}$	40.20°	139.06°	23	6.1
B	June 9, 1983	22 04 00.3	40.16	139.09	24	6.0
C	June 21, 1983	15 25 26.6	41.27	139.08	9	7.1

Table 1.   In Fig. 1, the fault model of the main shock by Shimazaki and Mori (1983) is also illustrated.   The figure shows that these three events occurred near the south edge or the north edge of the source area of the main shock.

We analyze intermediate-period P-wave records at 4 GDSN stations shown in Fig. 2.   The observation stations in which intermediate-period seismographs were installed are limited both in number and in azimuthal coverage around the epicenter of the event concerned.   Assuming that the earthquake source is represented by a point source, we aim at obtaining the moment rate function which describes the time history of wave-energy radiation from the source.   Figure 3 shows the P-wave records of long-period, intermediate-period and short-period seismometers of vertical component (LPZ, IPZ and SPZ) obtained for the three earthquakes at Red Lake, Ontario (RSON).   The amplitude units being arbitrary in this figure, comparison should be made only for the waveforms. Since the difference in epicenter location of the earthquakes is negligible in comparison with the epicentral distances of about 78 degrees to RSON, the difference of the waveforms is considered to be caused by differences in focal depth and in moment rate function.   The differences in waveform among the three events are more clearly seen on
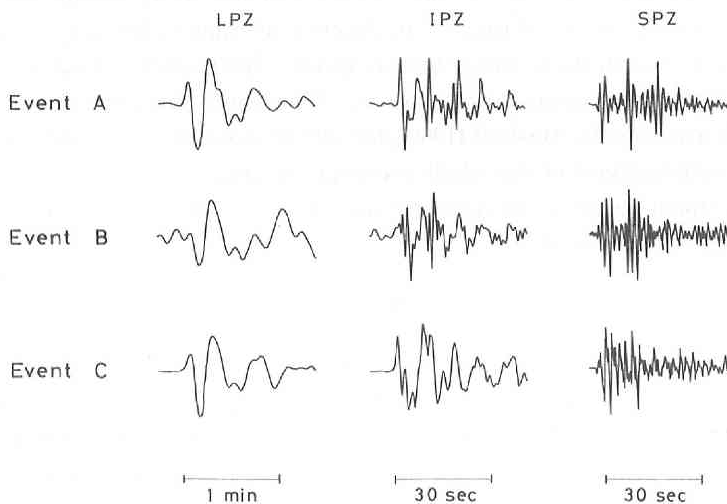

Fig. 3   Examples of P-wave records observed at RSON for the three events.   The amplitudes are in arbitrary units.   LPZ, IPZ and SPZ indicate long-period vertical component, intermediate-period vertical component and short-period vertical component.

IPZ records than on LPZ records.   We therefore expect that the source characteristics distinctive of the three events can be derived through the analysis of IPZ records.

The moment rate function, $m(t)$, is assumed to be expressed by a combination of ramp functions as

$$m(t) = \sum_{i=1}^{N} A_i s(t - t_i), \tag{1}$$

where N is the number of ramp functions. A_i and t_i are amplitude and delay time of each ramp function, and $s(t)$ is a unit ramp function with a rise time, τ ;

$$s(t) = \begin{cases} 0 & ; \quad t < 0, \\ t/\tau & ; \quad 0 \leq t < \tau, \\ 1 & ; \quad \tau \leq t. \end{cases} \tag{2}$$

The synthetic record $w(t)$, is calculated as

$$w(t) = (R_{\text{PZ}}/4\pi\rho a^3)(1/r_0)m(t) * G(t) * E(t) * H(t) * I(t), \tag{3}$$

where R_{PZ} is a conversion coefficient from the amplitude of incident P-wave to that of the vertical ground motion at an observation station, and ρ and a are the density and the P-wave velocity in the source region, respectively.   The term of $1/r_0$ represents the geometrical spreading effect along the wave propagation path.

$G(t)$ is a time function to express the sum of the direct P-wave and the reflected waves at the source region such as pP, sP and pwP waves. $G(t)$ should include the effect of the radiation pattern due to a double couple point source for each of the waves.   The crustal structure in the source region should be known to obtain $G(t)$, as will be shown in the following section. $E(t)$ is the term representing the attenuation of wave energy due to the inelastic medium property along the propagation path.   We calculate $E(t)$ by using the expression by Carpenter (1966).   In this calculation we assume the value of t^*, which is the ratio of the travel time to an effective average value of Q along the whole path, to be 0.7 sec for all the seismograms analyzed. $H(t)$ indicates the transfer function of the crust beneath an observation station.   We assume the same uni-layered crust model, which was used by Haskell (1960), for all the stations to calculate $H(t)$. $I(t)$ is the instrumental response of the whole recording system.

The agreement between the synthetic record, $w(t)$, and the observed record, $x(t)$, is measured with the parameter

$$\varepsilon = \int_0^T \{w(t) - x(t)\}^2 dt / \int_0^T \{x(t)\}^2 dt, \tag{4}$$

where T expresses the P-wave duration to be analyzed.

Assuming various values for the focal depth and the rise time, the unknown parameters of A_i and t_i in (1) are determined by minimizing ε for individual stations.   In doing this, we apply the procedure proposed by Kikuchi and Kanamori (1982) in their single-station analysis.   If the point source approximation is really valid for the wave-lengths of the observed P-waves under analysis, the moment rate functions obtained for individual stations should be identical with one another.   The reliability of the results in the

single-station analysis is therefore tested simply by the similarity of the unknown parameters estimated for individual stations.

3.   Focal Mechanism Solution and Crustal Structure

We have to know the focal mechanism solution of each event and the crustal structure in the source region in addition to the focal depth to calculate $G(t)$ in (3).   It is theoretically possible to determine these factors simultaneously with the moment rate function from the observed records.   In order to decrease the number of unknown parameters and have a better convergency, however, the mechanism solution and the crustal structure are estimated prior to a least squares procedure for obtaining the moment rate function and the focal depth.

The focal mechanism solutions of Events A and C are determined by a least squares method for S-wave data (Hirasawa, 1970).   The polarization angles of S-waves are read on long-period records at GDSN stations and illustrated by arrows in Fig. 4, where the lower half of the focal sphere is projected on an equal area net.   Since the S-wave records of Event B are disturbed by later phases of Event A that occurred about 15
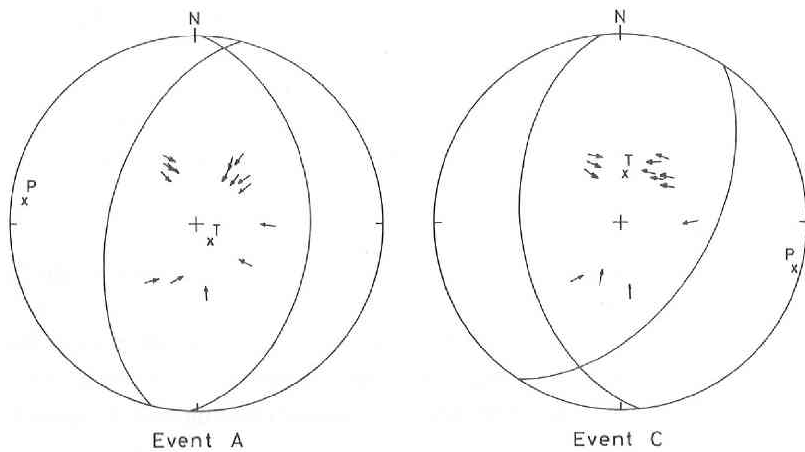

Event A   Event C

Fig. 4   Focal mechanism solutions for Events A and C.   The arrows indicate S-wave polariza-
tion angles.   The solid curves indicate the P-nodal planes obtained from the polarization
angles.   The number of observations used for the focal mechanism determination is 15 for
Event A and 13 for Event C.

Table 2.   Focal Mechanism Solutions

Event	Plane a		Plane b	
	dip direction	dip angle	dip direction	dip angle
A	91	39	284	52
B[1]	110	34	290	56
C	123	52	264	45

[1] obtained by Tohoku University from P-wave initial motion data.

Table 3.   Crustal Structure in Source Region

	Thickness (km)	P-wave velocity (km/sec)	S-wave velocity (km/sec)	Density (g/cm³)
Water	*	1.5	—	1.0
Sediment	2.0	2.5	1.4	2.3
Upper Crust	5.0	5.9	3.4	2.7
Lower Crust	7.0	7.0	4.0	3.0
Mantle	—	8.2	4.7	3.3

* 3.0 for Events A and B, and 1.5 for Event C.

minutes before Event B, the mechanism solution determined from the P-wave initial motions by the Tohoku University is adopted. The focal mechanism solutions of the three events are listed in Table 2.

Our crustal model for the source region is composed of four horizontally stratified layers; layers of water, sediment, the upper and the lower crust over the mantle. We adopt the result by Yoshii and Asano (1972) for P-wave velocity in each layer and the thicknesses of the upper and lower crusts. We obtain S-wave velocities from the assumption of the Poisson's relation and assume reasonable values for the density, as shown in Table 3. Since pwP-wave and reflected waves at the boundaries of the sediment layer would have significant effects on the waveforms of intermediate-period seismograms, we determine the thicknesses of water and sediment layers from the observed seismograms as described below.

The instrument of the IPZ component has a response characteristics proportional to the ground velocity in the period range from 1 to 20 sec. In the case of the IPZ record obtained for Event A at RSON, it is observed from Fig. 3 that the waveform of the first 3 sec from the onset is very simple and consists of a positive and a negative pulse of almost the same amplitude. This suggests that a single displacement pulse arrived at the station as the direct P-wave, and that the moment rate function for Event A can be
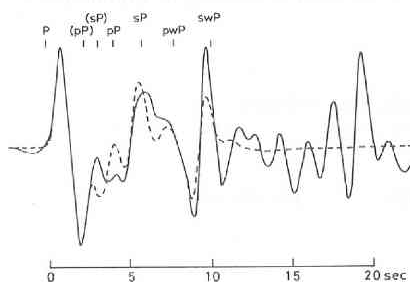

Fig. 5   Observed and synthetic records for an assumed moment rate function. The solid curve indicates the intermediate-period record observed at RSON for Event A. The dashed curve indicates the synthetic record by assuming a single trapezoid pulse for the moment rate function. The characters above the records indicate the arrival times of each phase in the synthetic record. P is the direct wave, (pP) and (sP) are reflected waves at the bottom of the sediment, pP and sP are those at the sea bottom, and pwP and swP are those at the sea surface.

approximated well by a single trapezoid function. From this we first assume a trial solution for the moment rate function of Event A as expressed by a trapezoid pulse of $A_1=7.5\times10^{24}$ dyne·cm/sec, $A_2=-7.5\times10^{24}$ dyne·cm/sec, $t_1=0$ sec, $t_2=1.0$ sec and $\tau=0.25$ sec. We next determine by the method of trial and error the focal depth and the thicknesses of water and sediment layers in the source region so that the synthetic wave for the trial solution may well account for the observation at RSON, where we pay particular attention to the arrival time differences among the direct P and prominent reflected phases. The best fit synthesized waveform thus obtained is shown in Fig. 5 in comparison with the observed one, where the focal depth determined is 13 km. The calculated arrival times of some prominent phases are indicated in the figure. The pwP-phase, which is one of reflected waves at the sea surface, should have a larger amplitude than any other reflected wave. The phase with large amplitude at about 8 sec after the direct P-phase on the observed record is regarded as the pwP-phase. If we assume a larger focal depth and attempt to identify the large phase at about 16 sce with the pwP-phase, the focal depth becomes deeper than 40 km and the prominent phase at 8 sec cannot be explained.

The thicknesses of water and sediment layers thus determined are given in Table 3. We use the same crustal structure both for Event A and for Event B, because the epicenter of Event B is very close to that of Event A. We assume the same crustal structure also for Event C except for water depth, which is estimated from the bathymetric chart.

4. Results

By minimizing ε defined in (4), we obtain from the observed records of GDSN the focal depth and the moment rate function of the three events including Event A. In this procedure, N in (1) is fixed to be 10 and t_i is restricted between 0 and 10 sec because the source process time would not be longer than 10 sec. The value of focal depth is varied from 6 to 30 km at every 1 km, and that of rise time is varied from 0 to 2 sec at every 0.25 sec. The record length to be analyzed is 25 sec from the P-wave onset.

Figure 6 shows the variation of ε with respect to the focal depth and the rise time, which is called ε-map henceforth. Although some secondary minima are seen in the figure, the cross indicates the point of the smallest value in ε at which the most probable values are estimated for the focal depth and the rise time. The focal depths of Events A and B are estimated consistently from the four observations to be 13 km and 12 km, respectively. In the case of Event C, however, the ε-maps do not have sharp troughs, though ε takes a minimum value at the focal depth of 8, 9 or 11 km. Considering the differences in magnitude of the three events, the source dimension of Event C should be significantly larger than those of Events A and B. The relatively large ambiguity in estimating the focal depth of Event C may be caused by the large source dimension.

Figures 7 through 9 show the best fit synthetic records and the estimated moment rate functions together with the observed records. In the case of Event A, nearly identical results are estimated from all the 4 stations; the estimated values of the focal
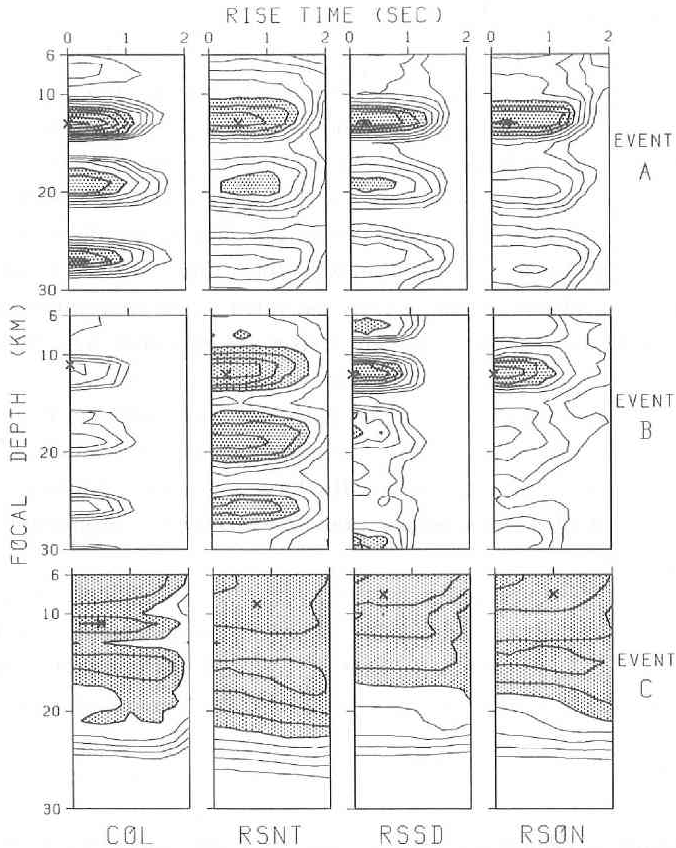
Fig. 6 Variation of ε with respect to the focal depth and the rise time. ε is the parameter measuring the agreement between observed and synthetic seismograms. The cross shows the focal depth and the rise time that give the minimum value of ε. The contour lines are drawn at every 0.05 interval for $\varepsilon \leq 0.7$. The regions where ε is smaller than 0.5 are stippled.

depth are the same 13 km and the estimated moment rate functions are similar in shape to one another, as shown in Fig. 7. The moment rate function of this event is thus simple and well approximated by a single trapezoid pulse with a duration time of about 1 sec, showing a good agreement with the trial solution and the focal depth determined preliminarily in the preceding section. This confirms the validity of our estimation for the crustal structure of the source region based on the trial solution.

On the other hand, the shape of the moment rate function estimated for Event B is complicated and varies from station to station, as seen in Fig. 8. Since the same moment rate function should be obtained for all the stations if the point source approximation is valid, this implies relatively poor reliability of the results. Nevertheless, it is clear that the moment rate function of this event consists of at least two main pulses, and the focal depth is about 12 km. It is noted that observed intermediate–period seismograms of Event B were contaminated by the long–period later phases of Event A that had
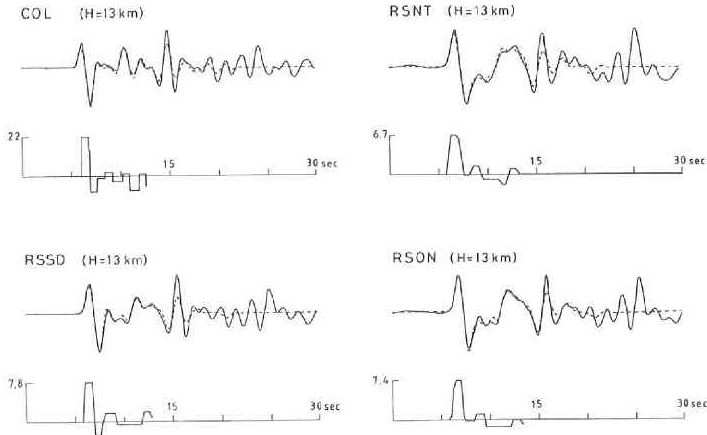
Fig. 7 Observed record, the best fit synthetic record and the moment rate function for Event A. H indicates the focal depth. The solid and dashed curves on the upper figure for each station indicate the observed record and the best fit synthetic record. The solid curve on the lower figure indicates the moment rate function. The amplitude unit of the moment rate function is 10^{24} dyne·cm/sec.

taken place about 15 minutes before Event B. This is one of reasons for the inconsistent results among the stations.

As stated before, the focal-depth resolution is poor for Event C. Nevertheless, the estimated moment rate functions are seen in Fig. 9 to be similar in shape to one another. Particularly for the three stations of RSNT, RSON and RSSD, the similarlity is very satisfactory. Neglecting the result of COL, we take 8 km as an approximate value of the focal depth.

The amplitude of the moment rate function estimated at COL is always much larger
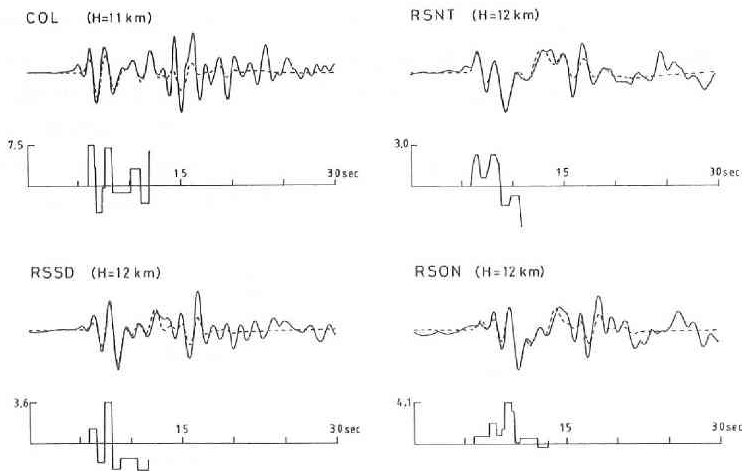

Fig. 8 Observed record, the best fit synthetic record and the moment rate function for Event B. The same convention is used as that in Fig. 7.
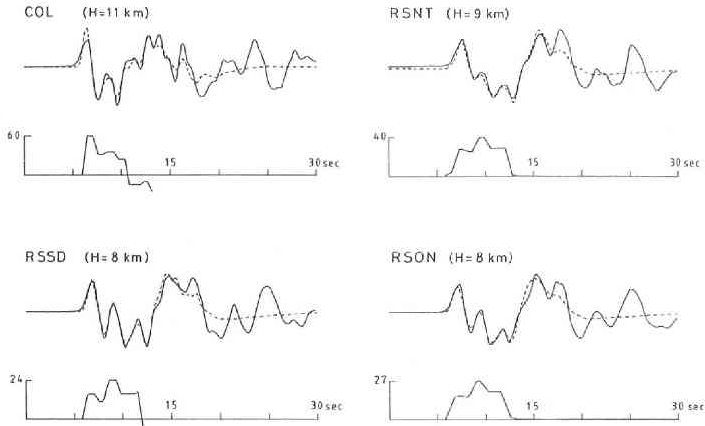
Fig. 9   Obsesved record, the best fit synthetic record and the moment rate function for Event
C.   The same convention is used as that in Fig. 7.

than those of the other stations, as seen in Figs. 7 to 9.   This may be attributed partly
to the inappropriate model of crustal structure beneath the station and partly to the
unsatisfactory assumption of constant t^* independent of epicentral distance.   The result
of COL is thus excluded in obtaining an average value of seismic moment.   By integrat-
ing the main part of the moment rate function, the average seismic moment is calculated
as 8×10^{24} dyne·cm for Event A, 7×10^{24} dyne·cm for Event B, and 1.2×10^{26} dyne·cm for
Event C.   It should be noted that these values were obtained from intermediate-period
records.   The results of the present section are summarized in Table 4.

Event A and Event B have nearly identical magnitude and almost the same
hypocenter location.   The difference in origin time between the two events is only about
15 minutes, as noted before.   However, the moment rate functions are very different
from each other.   The function of Event A suggests that the seismic waves were
generated by a rather simple process of faulting.   The main part of the moment rate
function is found to last only for about 1 sec, which is rather short for earthquakes with
magnitudes around 6.1.   If the source of Event A is assumed to be a circular crack with
a rupture velocity of 2.5 km/sec, the average stress drop on the circular fault of about
2.5 km in radius is 225 bars.   Since the rupture velocity estimated for the main shock
ranges from 1.5 km/sec to 2.5 km/sec (Sato, 1985 ; Fukuyama and Irikura, 1986), this

Table 4.   Source Characteristics

Event	Focal depth (km)	Seismic moment (dyne·cm)	Moment rate function	Process time (sec)
A	13	8×10^{24}	single pulse	1
B	12	7×10^{24}	double pulse (separated in time)	4
C	8	1.2×10^{26}	double pulse (not separated in time)	6

value of stress drop is considered the lower bound. This large stress drop may correspond not to the global stress drop but to the local stress drop on an asperity region of the fault. Similarly, the moment rate function of Event B suggests that two regions of asperity were ruptured separately in time. The moment rate function of Event C is found to be expressed by the sum of two trapezoid pulses with the same duration time of about 3.5 sec. In contrast to Event B, the two pulses are not separated in time; the time lag between them being about 2.5 sec.

5. Discussion

The sharp troughs in ε-maps for Events A and B in Fig. 6 indicate that the focal depths obtained in the present study are reliable. The focal depths estimated for Events A and B are significantly shallower than those determined by the Tohoku University as seen in Tables 1 and 4. The present results are consistent with the hypocenter distribution of aftershocks obtained by Sato et al. (1986).

Analyzing GDSN and WWSSN long-period SH-wave records, Masuda and Hamaguchi (1988) discussed the source processes of Events A and C by the second-central moment technique developed by Silver and Masuda (1985). The focal depths they estimated are 10 km for Event A and 9 km for Event C, showing a good agreement with our results. They determined the source process times as 4.1 sec for Event A and 6.0 sec for Event C. The process time for Event A is longer than ours. This difference is attributed to the difference in the periods of waves analyzed; long-period SH-waves and intermediate-period P-waves. This suggests that the process time obtained in the present study implies the rupture time of asperity.

Ishikawa et al. (1984) analyzed WWSSN long-period records of P-waves to study the source process of Event C. They found that a pre-event had occurred 2.5 sec before the main event. The time interval between them corresponds to the time lag of the two pulses obtained in the present study. The amplitudes of the main event was about ten times larger than that of the pre-event according to the result of Ishikawa et al. (1984). The present result, however, shows the amplitudes of the two events were almost the same as far as we deal with the seismic energy radiation in the period range between 1 and 20 sec.

The two aftershocks of Event A and Event B are similar to each other in their hypocenter locations, in their magnitudes and in their focal mechanism solutions. As described in the preceding section, however, a large difference between the two events are found for their source processes. Accelerograms of the two events were obtained at Akita by the Port and Harbour Research Institute (Kurata et al., 1983) as shown in Fig. 10. The distances between Akita and the epicenters of the events are about 100 km. The envelope of the accelerograms for Event A shows, relatively speaking, an abrupt increase in amplitude while that for Event B shows a gradual increase. Since the hypocenters of the two events are close to each other, the effects of the wave propagation path from the source to Akita station can be regarded as the same for the two events. In order to remove the effect of the wave propagation path, the spectral ratio of Event
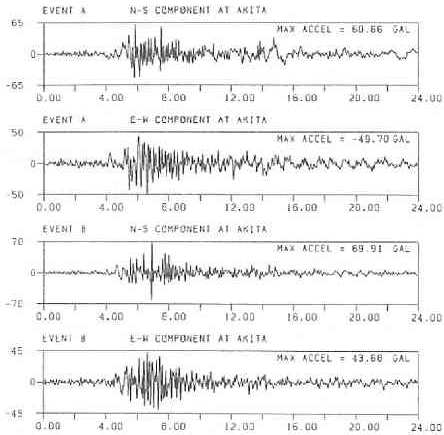
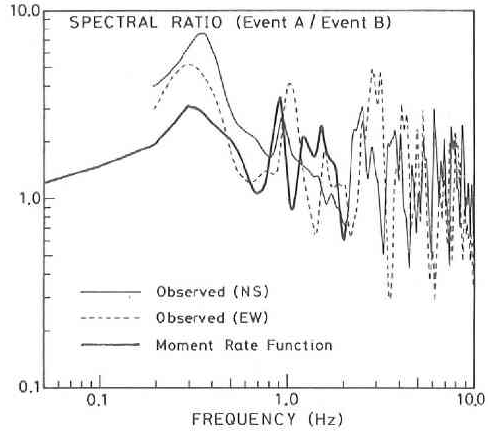Fig. 10   Accelerograms for Events A and B recorded at Akita.

Fig. 11   Ratio of Fourier spectra for Event A to those for Event B. The thin solid curve and the dashed curve indicate the spectral ratios for the accelerograms observed at Akita. The thick solid curve indicates the spectral ratio of the moment rate function estimated for RSON.

A to Event B is computed for the observed accelerograms. The result is compared in Fig. 11 with the spectral ratio of moment rate functions between the two events. The reliable frequency ranges for the ratios are limited by the characteristics of the recording instruments to be from 0.2 to 10 Hz for the accelerograms and from 0.05 to 2 Hz for IPZ records. The spectral ratio of the moment rate function accounts fairly well for those of the observed ground acceleration in the frequency range between 0.2 and 2 Hz. It is concluded that the strong ground motions at Akita were strongly affected by the source process.

Recently, the semi-empirical method was developed for prediction of strong ground motion (e.g., Irikura, 1983; Takemura and Ikeura, 1988). Accelerograms from earthquakes smaller in magnitude than a target earthquake are regarded as empirical Green functions and superposed to obtain synthetic accelerograms for the large target earthquake. The present results indicate that the seismograms obtained for Event A can be regarded as empirical Green functions while those for Events B and C cannot. We have to pay attention to the source process of small earthquakes in applying the empirical Green function method.

References

Carpenter, E.W., 1966: Absorption of elastic waves — An operator for a constant Q mechanism, *Rep. O-43/66, At. Weapons Res. Estab., London*, 1-16.

Fukuyama, E. and K. Irikura, 1986: Rupture process of the 1983 Japan Sea (Akita-Oki) earthquake using a waveform inversion method, *Bull. Seism. Soc. Am.*, **76**, 1623-1640.

Haskell, N.A., 1960: Crustal reflection of plane SH waves, *J. Geophys. Res.*, **65**, 4147-4150.

Hirasawa, T., 1970: Focal mechanism determination from S wave observations of different quality, *J. Phys. Earth*, **18**, 285-294.

Irikura, K., 1983: Semi-empirical estimation of strong ground motions during large earthquakes, *Bull. Disas. Prev. Res. Inst., Kyoto Univ.*, **33**, 63-104.

Ishikawa, Y., M. Takeo, N. Hamada, M. Katsumata, K. Satake, K. Abe, M. Kikuchi, K. Sudo, M. Takahashi, S. Kashiwabara, and N. Mikami, 1984: Source process of the Japan Sea earthquake of 1983, *Chikyu*, No. 55, 11-17 (in Japanese).

Kanamori, H. and L. Astiz, 1985: The 1983 Akita-Oki earthquake ($M_w = 7.8$) and its implication for systematics of subduction earthquakes, *Earthq. Predict. Res.*, **3**, 305-317.

Kikuchi, M. and H. Kanamori, 1982: Inversion of complex body waves, *Bull Seism. Soc. Am.*, **72**, 491-506.

Kurata, E., T. Fukuhara, and S. Noda, 1983: Strong-motion earthquake records on the 1983 Nipponkai-Chubu earthquake in port areas, *Tech. Note Port Harbour Res. Inst.*, No. 458, 1-372.

Masuda, T. and H. Hamaguchi, 1988: Source process of the 1983 Japan Sea earthquake and its large aftershocks, *Prog. Abstr. Seismol. Soc. Japan*, No. 2, 4 (in Japanese).

Nakamura, K., 1983: Possible nascent trench along the eastern Japan Sea as the convergent boundary between Eurasian and North American plates, *Bull. Earthq. Res. Ints.*, **58**, 711-722 (in Japanese with English summary).

Nosaka, M., K. Suyehiro, and T. Urabe, 1987: Aftershock distribution of the 1983 Japan Sea earthquake derived by ocean-bottom and land based station, *J. Phys. Earth*, **35**, 209-224.

Sato, T., 1985: Rupture characteristics of the 1983 Nihonkai-Chubu (Japan Sea) earthquake as inferred from strong motion accelerograms, *J. Phys. Earth*, **33**, 525-557.

Sato, T., M. Kosuga, K. Tanaka, and H. Sato, 1986: Aftershock distribution of the 1983 Nihonkai-Chubu (Japan Sea) earthquake determined from relocated hypocenters, *J. Phys. Earth*, **34**, 203-223.

Shimazaki, K. and J. Mori, 1983: Focal mechanism of the May 26, 1983 Japan Sea earthquake, *Prog. Abstr. Seosmol. Soc. Japan.* No. 2, 15.

Silver, P. and T. Masuda, 1985: A source extent analysis of the Imperial Valley earthquake of October 15, 1979, and the Victoria earthquake of June 9, 1980, *J. Geophys. Res.*, **90**, 7639-7651.

Takemura, M. and T. Ikeura, 1988: A semi-empirical method using a hybrid of stochastic and deterministic fault models: Simulation of strong ground motions during large earthquakes, *J. Phys. Earth*, **36**, 89-106.

Umino, N., A. Hasegawa, K. Obara, T. Matsuzawa, H. Shimizu, and A. Takagi, 1985: Hypocenter distribution of foreshocks and aftershocks of the 1983 Japan Sea earthquake, *Zisin, Ser. 2*, **38**, 399-410 (in Japanese with English abstract).

Urabe, T., K. Suyehiro, T. Iwasaki, N. Hirata, T. Kanazawa, A. Nishizawa, and H. Shimamura, 1985: Aftershock distribution of the 1983 Japan Sea earthquake as determined from helicopter-dispatched OBS observation, *J. Phys. Earth*, **33**, 133-147.

Yoshii, T. and S. Asano, 1972: Time-term analysis of explosion seismic data, *J. Phys. Earth*, **20**, 47-57.